Electronic inhomogeneity and phase fluctuation in one-unit-cell FeSe films

Dapeng Zhao [1,6], Wenqiang Cui [1,2,6], Yaowu Liu[2,6], Guanming Gong[2], Liguo Zhang [1], Guihao Jia[2], Yunyi Zang[1], Xiaopeng Hu[2], Ding Zhang [1,2,3], Yilin Wang [4] ✉, Wei Li[2,3], Shuaihua Ji [2,3], Lili Wang [2,3] ✉, Ke He [1,2,3], Xucun Ma[2,3] & Qi-Kun Xue[1,2,3,5] ✉

One-unit-cell FeSe films on $SrTiO_3$ substrates are of great interest owing to significantly enlarged pairing gaps characterized by two coherence peaks at ±10 meV and ±20 meV. In-situ transport measurement is desired to reveal novel properties. Here, we performed in-situ microscale electrical transport and combined scanning tunneling microscopy measurements on continuous one-unit-cell FeSe films with twin boundaries. We observed two spatially coexisting superconducting phases in domains and on boundaries, characterized by distinct superconducting gaps (Δ_1~15 meV vs. Δ_2~10 meV) and pairing temperatures (T_{p1}~52.0 K vs. T_{p2}~37.3 K), and correspondingly two-step nonlinear $V \sim I^\alpha$ behavior but a concurrent Berezinskii–Kosterlitz–Thouless (BKT)-like transition occurring at T_{BKT}~28.7 K. Moreover, the onset transition temperature T_c^{onset}~54 K and zero-resistivity temperature T_c^{zero}~31 K are consistent with T_{p1} and T_{BKT}, respectively. Our results indicate the broadened superconducting transition in FeSe/$SrTiO_3$ is related to intrinsic electronic inhomogeneity due to distinct two-gap features and phase fluctuations of two-dimensional superconductivity.

Superconducting transition temperature (T_c) marks the inception of a macroscopic quantum phase-coherent paired state in fermionic systems. The paired fermionic system is described in a weak coupling Bardeen–Cooper–Schrieffer (BCS) limit or a strong coupling Bose–Einstein condensation (BEC) limit, scaled with a criterion $c \equiv 1/(k_F \xi_{pair}) \sim \frac{E_F^{1-6}}{\Delta}$. Here, k_F is the Fermi momentum, ξ_{pair} is the coherence length, Δ is the superconducting gap, and E_F is the Fermi energy. Between these two limits, namely, the BCS-BEC crossover regime, incoherent fermion pairing occurs due to the Fermi surface instability at a pairing temperature T_p, forming the so-called pseudogap phase, while superfluidity of coherent pairs occurs at a lower temperature T_c. Given the characteristic superconducting gap magnitude Δ ~15–20 meV and the relatively small Fermi energy

E_F~56 meV, one-unit-cell (1 UC) FeSe on $SrTiO_3$(001) resides in the BCS-BEC crossover regime[5–7]. In coincidence with the crossover scenario, the hitherto observed zero-resistance temperature T_c^{zero} of 20–30 K is much lower than the pairing temperature T_p of 50–83 K, as disclosed by angle-resolved photoemission spectroscopy (ARPES) investigations[8–15].

The two-dimensional (2D) limit is a distinct feature of monolayer FeSe that relates closely to superfluidity. In strictly 2D, topological vortex-antivortex phase fluctuations give a Berezinskii–Kosterlitz–Thouless (BKT) transition[16–19]. The superfluidity disappears when the phase correlations change from a quasi-long range to short range order via the vortex-antivortex unbinding at a critical temperature T_{BKT}. Within the ideal BKT scenario, the $V(I)$

characteristics exhibit $V \sim I^{\alpha}$ power-law dependence, and the exponent α jumps discontinuously from 3 to 1 upon the temperature approaching T_{BKT} from the lower side[20]. Indeed, previous $V \sim I^{\alpha}$ results indicate a BKT-like transition at a T_{BKT} ($\alpha = 3$)-T_c^{zero}-23 K[9]. However, in sharp contrast to the full linear behavior within $1.1T_{BKT}$ for conventional superconductor films[21], the component α gradually decays to 1 until above $1.3T_{BKT}$, suggesting different mechanisms.

The coupling with the oxygen-deficient TiO_2 layer gives rise to the unique enhanced pairing in the 1 UC FeSe, characterized by double-gaps with two pairs of coherence peaks, namely one pair defined as inner gap at ± 10 meV and the other pair as outer gap varying within ± 15–20 meV[8,22]. The interfacial coupling strength and, thus, the pairing strength sensitively depends on the local interface stoichiometry, particularly the delicate competition between electron-doping from oxygen vacancies and hole-doping from extra Se adatoms[23,24]. Under the strong interface coupling limit, the 1 UC FeSe film consists of domains with diameters below hundred nanometers separated by unidirectional line defects, wherein the outer gap reaches at 20 meV in maximum. However, the gap magnitude decreases with reduced domain size and even vanishes in isolated domains with diameter below ~20 nm[25]. Besides the random and drastic variation of pairing gaps in the sub-micron scale, the pairing gaps exhibit lateral gradient reduction of ~2 meV per millimeter, resulting from the lateral oxygen gradient accumulation due to their spontaneous flow under the electric field[23]. Indeed, previous ARPES measurements from different groups reported varied gap magnitude Δ ~10–15 meV and pairing temperature T_p-50–83 K, due to the delicate interface coupling and strong spatial inhomogeneity.

In this work, we performed in-situ combined STM/STS and micron-scale electrical transport measurements and directly collected the spatially resolved pairing gaps and coherent pairing behavior in 1 UC FeSe. The micro-scale probes help to reduce the lateral pairing deviation due to the gradient distribution of oxygen vacancies. To reduce the sub-micro scale inhomogeneity, we prepared morphologically continuous 1 UC FeSe films on Nb-SrTiO$_3$(001) (0.7 wt %) under Se relatively rich condition, at the expense of weakened interface coupling featured by a maximum pairing gap of ~15 meV (for details, see Supplementary Figs. S1 and S2). Our results demonstrate the 1 UC FeSe with twin boundaries as a percolative system of two superconducting phases with Δ_1-15 meV and Δ_2-10 meV, exhibiting two-step nonlinear $V \sim I^{\alpha}$ behavior with contrasting α-T relations at low current and high current regimes.

Results

STM characterization of 1 UC FeSe

Figure 1a displays the topographic image of morphologically continuous 1 UC FeSe films following the terrace-step structure of the SrTiO$_3$(001) surface, with domains of several to tens of nanometers wide on terraces split by wavy bright boundaries. The zoom-in atomically resolved image displayed in Fig. 1b reveals structurally continuous Se-terminated (001) lattices over the whole surface with expanded Se(001) lattice (3.82 ± 0.05 Å), compared with bulk FeSe. A detailed insight into the atomic structure around the boundary gives inversed lattice anisotropy in the adjacent domains, as marked by flipped white/yellow arrows ($a_0 > b_0$), and compressed in-plane Se(001) lattice (3.70 ± 0.05 Å) in the $4a_0$–$6a_0$ wide boundary and lattice shifts upon merging, as illustrated by the staggered blue lines in the right panel. The above features indicate a twin boundary.

The contrasting lattice on boundaries induces varied pairing. Figure 1c shows the tunneling spectra taken across the boundaries at the locations labeled as colored dots in Fig. 1b. The superconducting gap reaches ~15 meV for regions away from the boundary, and reduces to ~10 meV in magnitude with significantly reduced coherence peaks and spectra weight loss due to pairing in 3 nm wide region spanned the border (the middle there curves). The 1 UC FeSe films with dense twin

boundaries can be regarded as a spatially percolative system consisting of two superconducting phases characterized by the respective superconducting gaps Δ_1-15 meV and Δ_2-10 meV.

Figure 1d, e shows the typical temperature-dependent dI/dV spectra taken in domains and on boundaries, respectively. The superconducting gap magnitudes are Δ_1-15 meV and Δ_2-10 meV at 5.0 K. With increasing temperature, the gaps fill up, that is, coherence peaks maintain at $\pm\Delta_1$ and $\pm\Delta_2$, but the intensities gradually reduce and remain discernable till 32 K and 34 K, respectively, while the gaps remain visible until 50 K and above 34 K. No reliable spectrum is obtainable above 50 K due to thermal drift in our STM system. Figure 1f, g summarizes the corresponding temperature-dependent gap magnitude (blue squares) deduced from the BCS fitting (Supplementary Fig. S3b) and gap height (orange circles) defined as the difference between negative-bias coherence peak and zero bias conductance (exemplified by the arrowed dash in Fig. 1d). The blue and orange dashed lines correspond to the BCS fitting of gap magnitude (based on BCS gap function, see Supplementary Fig. S3b) and the linear fitting of gap height, respectively. The fittings on gap magnitude and gap height yield consistent T_{p1}-52.0 K and T_{p2}-37.3 K. Notably, the coherence peak of the superconducting gap ~15 meV vanishes at ~32 K (Fig. 1d and Supplementary Fig. S3a). We define this temperature as T_{cp}.

In-situ micron-scale electrical transport measurement of 1 UC FeSe

Then we performed in-situ micron-scale electrical transport measurements to characterize the microscopic coherence. The silicon cantilevers coated with Au/Ti, as illustrated in Fig. 2a, b, directly contact the sample surface with an inter-probe separation of 5 μm. Under such a micro-scale soft contact, the current flows mainly through the thin surface layer, enabling the collection of electrical transport dominantly from the FeSe films rather than Nb-doped SrTiO$_3$ substrates (Supplementary Fig. S4). Figure 2c displays a typical temperature-dependent resistance (R-T) curve, with the temperature-dependent gap magnitude inserted for comparison. The resistance starts to decrease at $T_c^{onset} = 54.0$ K and drops completely to zero (defined as resistance within the instrumental resolution of $\pm 0.01 \Omega$) at $T_c^{zero} = 31.0$ K. The crossing point between the linear extrapolation of the normal state and the superconducting transition is 43.8 K. Moreover, the zero-resistance state below $T_c^{zero} = 31$ K is further confirmed by the temperature-dependent V-I behaviors shown in Fig. 2d. The V-I curves at low temperatures show an apparent superconducting current plateau which becomes progressively shorter with increasing temperature and vanishes at approximately 31 K. The onset temperature T_c^{onset}-54.0 K and the zero-resistance temperature T_c^{zero}-31.0 K are consistent with T_{p1} and T_{cp}, respectively, within experimental uncertainty. Note that under strong interface coupling, one can speculate a high T_c^{onset} as well as the pairing temperature in 1 UC FeSe with the superconducting gap ~20 meV, which deserves further in-situ investigations (for details, see Supplementary Table S3).

We then check the $V(I)$ characteristics to gain deep insight into the transition region. Figure 3a summarizes the $V(I)$ curves on a double-logarithmic scale under temperatures varying from 19 to 35 K. Below 30 K, the $V(I)$ curves exhibit a two-step power-law $V \sim I^{\alpha}$ dependences, marked as regime H (high-current) and L (low-current), respectively, connected by a plateau marked in gray shadow. As the temperature increases, the plateau becomes progressively shorter until it vanishes at approximately 29 K. The α-exponents are extracted from the power-law fittings in the two regimes respectively, as marked by short black dashed lines. Figure 3b presents detailed evolutions of the α-exponents as a function of temperature. With decreasing temperature, the exponent α in the high current regime deviates from 1 at 30 K and approaches 3 at $T_H = 28.1$ K. At temperatures above 30 K, the $V(I)$ differs from the linear dependence and exhibits $\alpha < 1$. In contrast, the low current regime exhibits a broader transition and weaker exponent

variation: the exponent α deviates from 1 at a consistent temperature as regime H, approaches 3 at $T_L = 24.0$ K, and then fluctuates around 4 at lower temperatures. On the other hand, the observed $R(T)$ characteristics are consistent with a BKT transition. Close to T_{BKT}, the resistance follows the Halperin–Nelson equation $R(T) = R_0 \exp[-b(T/T_{BKT} - 1)^{-1/2}]$, where b is a material parameter[26]. As shown in Fig. 3c, the $(d\ln R/dT)^{-2/3}$ versus T curve deviates from the linear relation at ~31 K and yields T_{BKT} ~28.7 K, agreeing well with T_H.

The two-step power law $V \sim I^{\alpha}$ dependences evidence percolation via a network of superconducting puddles with different pairing strengths, echoing the two contrasting superconducting phases with Δ_1 ~15 meV and Δ_2 ~10 meV shown in Fig. 1. Within the BKT scenario, the α-exponent $\alpha(T) = 1 + \frac{\pi J_s(T)}{T}$, where J_s is superfluid phase stiffness, $J_s = \hbar^2 n_s/4m = \hbar^2 c^2 d/16\pi e^2 \lambda^2$, with n_s the 2D superfluid density, λ the penetration depth, and d the film thickness[20]. In an ideal BKT transition, the α-exponent jumps discontinuously from 3 to 1 with the temperature from T_{BKT}^- to T_{BKT}^+, correspondingly, $J_s(T)$ from $\frac{2}{\pi}T_{BKT}$ to 0. Beyond the ideal discontinuous α-exponent jump due to BKT transition, finite-size effect and inhomogeneity generally induce the broadening of the BKT transition[20]. Given the contrasting features in high-current and low-current regimes, the α-exponent transition in the former is closer to an ideal BKT transition. It is also supported by the $(d\ln R/dT)^{-2/3}$-T analysis, giving consistent T_{BKT} ~28.7 K with the V-I^{α} feature in the high-current regime. Notably, the $0.06T_{BKT}$ transition is sharper than all the previous observations in 1 UC FeSe and SrTiO₃-based heterostructures[9,19]. Moreover, it is comparable to conventional 2D superconductors[21], indicative of improved homogeneity. With increased portions lost superconductivity under high current and high temperature, the current partially flows through the conductive substrate beneath the FeSe film, inducing trivial α < 1. The relatively broad transition in the low-current regime is likely due to the weak superconductivity in the weak superconducting puddles with much lower superfluid phase stiffness J_s.

Figure 4a shows the R-T curves of 1-3 UC FeSe films, with T_c^{onset} and T_c^{zero} plotted as a function of film thickness. With increasing film thickness, the normal state resistivity decreases gradually, whereas the T_c^{onset} significantly decreases with the second UC FeSe overlaid but varies little upon further FeSe deposition. Another more striking

feature is that the T_c^{zero} remains at 31 K. This special thickness-dependent behavior demonstrates unique superconductivity in 1 UC FeSe rather than multilayer FeSe films, because the latter only contributes normal state conductivity but does not reduce superconducting fluctuation, which is the key factor to determine T_{BKT} and thus T_c^{zero}. The significant decrease of T_c^{onset} upon additional FeSe overlaid can be interpreted by weakened electron doping and strain effect in the monolayer FeSe, as disclosed by previous ARPES investigations[11]. The rich Se flux applied for tetragonal FeSe films deposition introduces hole doping to counteract the original electron doping. On the other hand, the overlayer FeSe films counteract the in-plane expansion enforced by the STO substrate.

Discussion

Combined with previous ARPES characterization on the Fermi surface of 1 UC FeSe and the contrasting dI/dV spectra on domains and boundaries, we present a comprehensive picture to depict the superconducting behavior of FeSe/SrTiO₃. The 1 UC FeSe with twin boundaries is a percolative system consisting of two superconducting phases, as illustrated in Fig. 4b. Compared with the phase with Δ_1 ~15 meV in domains, the phase with Δ_2 ~10 meV on boundaries exhibits blue-shifted kink of the valence band (for details, see Supplementary Fig. S5), corresponding to reduced electron pockets at M point[27], as illustrated in Fig. 4c, d.

Given the continuous 1 UC FeSe films and the minor content (<10%) of twin boundaries, as exemplified in Fig. 1a, the domains with Δ_1 ~15 meV dominate the transport behavior, particularly under the superconducting state. This view is supported by the finding that T_c^{zero} and T_c^{onset} from global transport measurements are consistent with T_{cp} and T_{p1} from local spectroscopy measurements in domains, respectively. Moreover, the sharp BKT-like transition disclosed from the $V(I)$ behavior gives a T_{BKT} close to T_{cp}. Right below T_{BKT}, zero resistivity is obtained, indicating a series of connected domains under the phase-coherent macroscopic quantum state. As the temperature reaches T_{BKT}, the proliferation of free topological vortices within the system leads to a sudden reduction of the superfluid density, concurrent with fluctuating coherence peaks and vanishing zero-resistivity. Since vortex dynamics is extremely disorder-sensitive in the 2D limit, the
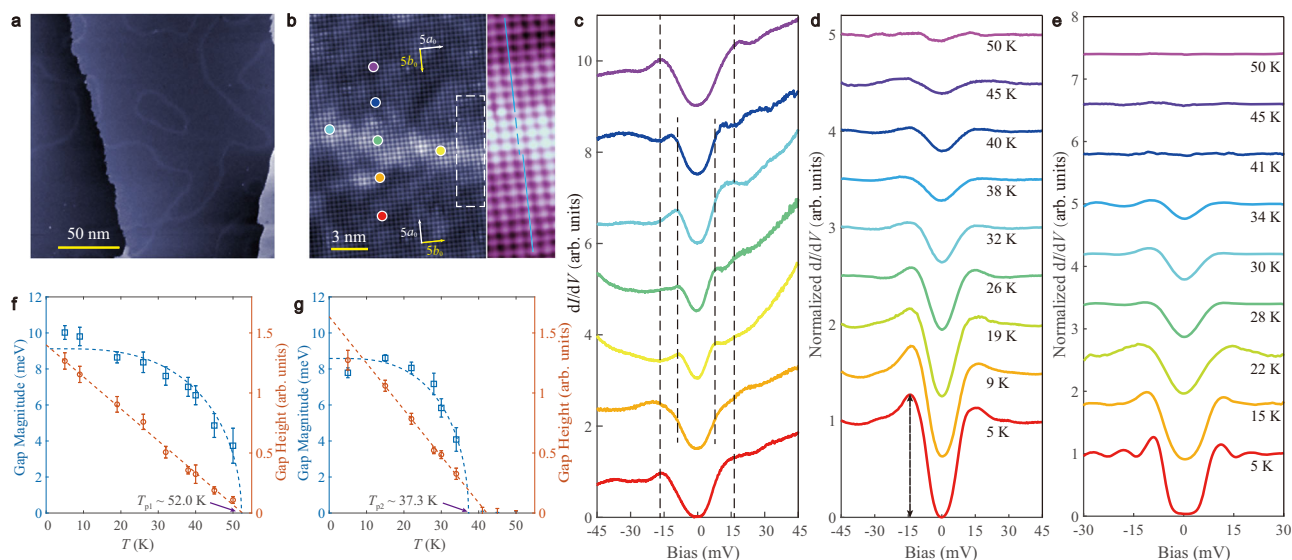

Fig. 1 | STM characterization of 1 UC FeSe/SrTiO₃(001). a Large-scale (sample bias $V_S = 1$ V, tunneling current $I_t = 10$ pA) and **b** zoom-in atomically resolved ($V_S = 0.1$ V, $I_t = 300$ pA) topographic images. **c** The dI/dV tunneling spectra taken at the locations marked by colored dots in **b**. (set point: $V_S = 45$ mV, $I_t = 200$ pA, $\Delta V = 0.5$ mV). Temperature-dependent dI/dV spectra taken **d** in domains (set point: $V_S = 45$ mV,

$I_t = 200$ pA, $\Delta V = 0.5$ mV) and **e** on twin boundaries (set point: $V_S = 30$ mV, $I_t = 200$ pA, $\Delta V = 0.5$ mV). The spectra are normalized by dividing the raw spectra by their backgrounds obtained with the extrapolated method. **f, g** The gap magnitude and gap height of the dI/dV spectra in **d** and **e** as a function of temperature, respectively. The error bars are from the s.d. of the fittings.
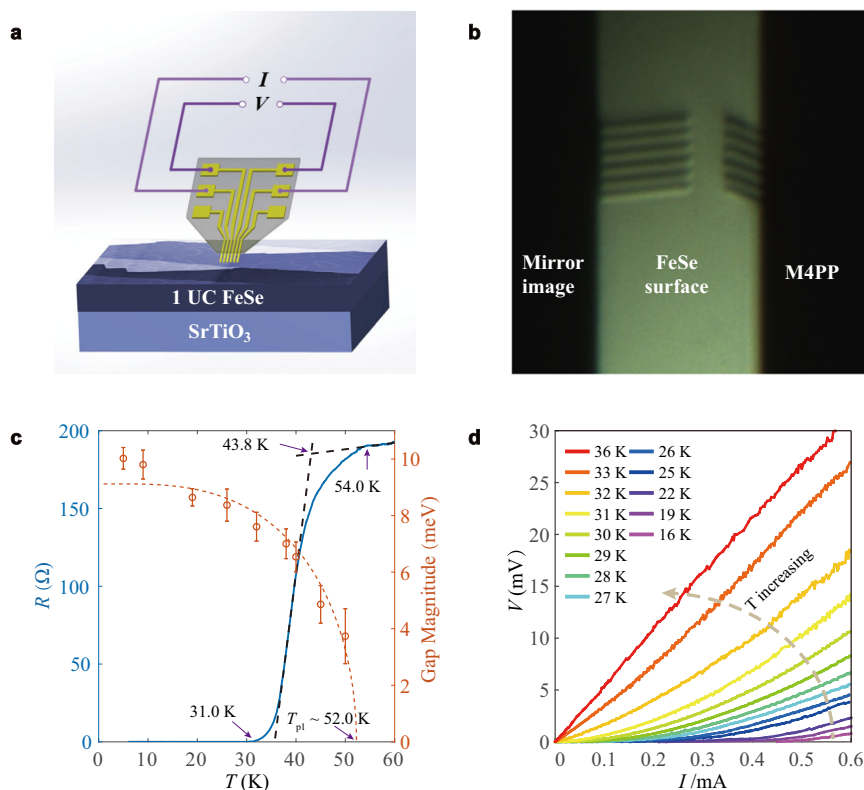
Fig. 2 | In-situ micron-scale electrical transport measurements of 1 UC FeSe/ SrTiO₃. a Schematic of the measurement setup. **b** Optical image of the contacting process. The probes are spaced apart by 5 µm. The angle between probes and the sample surface is 30°, which allows soft contacts. **c** The resistance and the gap magnitude as a function of temperature, indicating the onset resistance-drop temperature agrees well with T_{p1}. **d** V-I curves at fixed temperatures from 16 K to 36 K, showing a superconductor-metal transition at ~31 K.

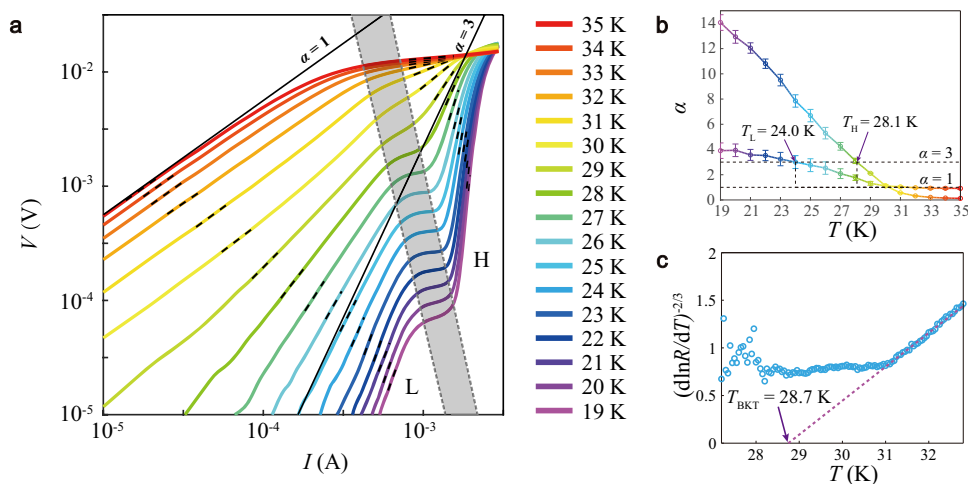**Fig. 3 | BKT transition in FeSe/SrTiO₃. a** $V(I)$ characteristics from 19 K to 35 K on a double-logarithmic scale. Two solid lines correspond to $V \sim I$ and $V \sim I^3$ dependences, respectively. **b** Temperature evolution of the exponent α, extracted from the power-law fittings in regimes H and L in **a** giving $T_H = 28.1$ K and $T_L = 24.0$ K when α = 3. The error bars are from the s.d. of the fittings. **c** Temperature dependence of $(d\ln R/dT)^{-2/3}$. The purple dashed line shows the fitting to the Halperin–Nelson equation with T_{BKT} ~28.7 K.

electronic inhomogeneity around the boundaries limits T_{BKT} in 1 UC FeSe[20,28–31]. Upon either increased temperature or increased current, the superconductivity is destroyed locally around the boundaries with weak superfluid phase stiffness, and then in domains till the complete loss of superconductivity at T_c^{onset}, in coincidence with the gap closing temperature T_{p1}. The above picture is further supported by the two-step $V(I)$ behavior with a clear intermedia plateau, with the low-current

and high-current regimes dominated by the boundary and domain phases, respectively. In contrast, the R-T behavior exhibits a wide transition in the temperature range between T_{cp} and T_{p1}.

Moreover, a previous study on the highly two-dimensional bulk superconductor (TBA)ₓFeSe, where the distance between adjacent FeSe layers is enlarged from ~5.5 Å in pristine FeSe to 15.5 Å by TBA⁺ intercalation, exhibits a sharper superconducting transition than 1 UC
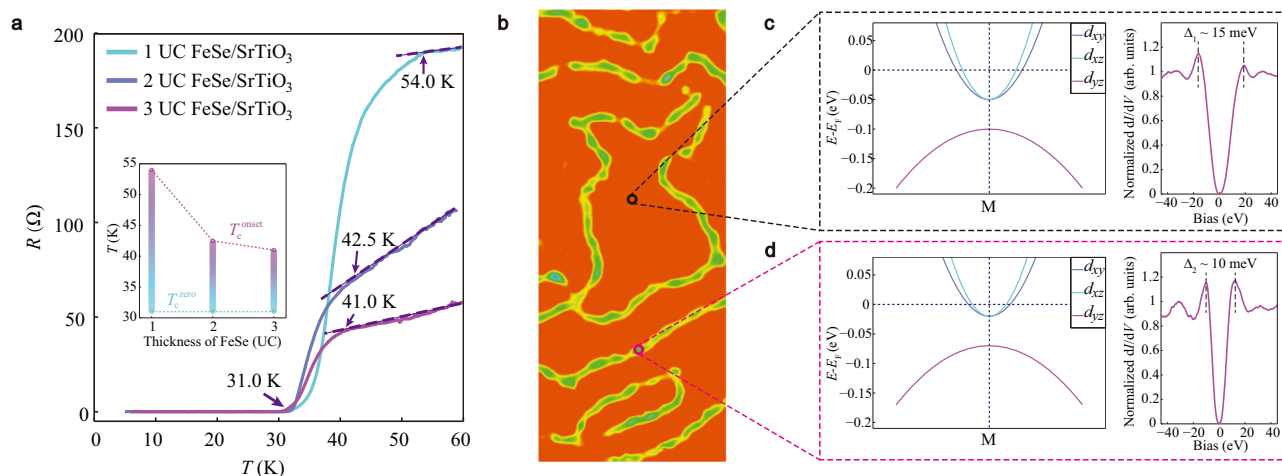
Fig. 4 | Thickness variation and electronic inhomogeneity of FeSe/SrTiO₃. a The resistance of 1-3 UC FeSe films as a function of temperature. The inset shows T_c^{onset} and T_c^{zero} as a function of film thickness. **b** Schematic illustrating the electronic inhomogeneity of FeSe/SrTiO₃. The orange area represents the superconducting

phase with Δ_1 ~15 meV and the green area represents the superconducting phase with Δ_2 ~10 meV. **c, d** Schematic of band structures at M point and representative dI/dV spectra of two superconducting phases of 1 UC FeSe/SrTiO₃.

FeSe[32]. The onset temperature where the resistance starts to decrease is ~55 K, and T_c^{zero} (~T_{BKT}) is ~43 K. The prominent difference between this system and 1 UC FeSe/SrTiO₃ is the lack of domains, which echoes that the electronic inhomogeneity around domain boundaries in 1 UC FeSe contributes to the broadening of superconducting transition.

It is worth noting that the 1 UC FeSe is characterized by a two-gap feature with robust inner gap at ±10 meV and sensitively varied outer gap within ±15–20 meV, while the Δ_2 ~10 meV universally observed on twin boundaries agrees well with the inner gap value. Despite the missed two-gap feature in this work due to the reduced energy resolution[22] (increased oscillation under in-situ transport system combination), the unique two-step $V(I)$ features we presented here suggest electronic percolation system as well. The two-gap features and the pairing mechanism remain elusive. The results of this work may invoke more investigation and vision on the multiple-orbital properties in iron-based superconductivity[33–37].

In summary, we establish the direct comparison between spatially resolved spectroscopic probes on pairing and transport behavior of 1 UC FeSe/SrTiO₃ with twin domain boundaries by combining STM/STS and micron-scale electrical transport measurement technique under the same ultra-high vacuum. Our results reveal that the spatial electronic inhomogeneity and phase fluctuations cooperatively determine the transport behavior of FeSe/SrTiO₃. The former contribution is non-ignorable, but unfortunately underestimated in previous works. The in-situ combined spatially resolved spectroscopy and transport techniques presented in this work pave the way for eventually disclosing the pairing and coherence scenario in high-temperature superconductivity.

Methods

Our experiments were conducted in a homemade ultra-high vacuum low-temperature STM - in-situ micron-scale electrical transport combined system, equipped with molecular beam epitaxy (MBE) and reflection high-energy electron diffraction (RHEED) for film preparation under the in-situ surface morphology monitor[38] (Supplementary Fig. S6). The base pressure is better than 1.0×10^{-10} Torr. The Nb-doped SrTiO₃(001) (0.7 wt %) substrates were degassed at 600 °C for hours and then annealed at 1200 °C for 20 min to get atomically flat surfaces. FeSe films were then grown by co-evaporating high-purity Fe (99.995%) and Se (99.9999%) from standard Knudsen cells under Se-rich conditions as the substrate was heated to 420 °C. The growth rate is ~0.05 UC/min. At last, the samples were annealed at 460 °C for hours. The RHEED images (Supplementary Fig. S2) indicate a highly flat

SrTiO₃(001) surface and the epitaxial growth of single-crystalline FeSe films aligned with the SrTiO₃ substrates. All STM data were collected in a constant current mode at 5.0 K using polycrystalline PtIr tips calibrated on Ag films. The dI/dV spectra were measured using a standard lock-in technique with a bias modulation of 0.5 mV at 973 Hz. In-situ electrical transport measurements based on the micro-four-point probe (M4PP) approach developed by Hasegawa et al. were performed under a built-in Pulse Delta measurement mode of Keithley Source-Meters 6221/2182 A with a pulsed current I = 2 μA applied[39,40] (Supplementary Fig. S7).

Data availability

All data supporting the findings of this study are available within the paper and/or the Supplementary Information. Any additional requests for information of this study are available from the corresponding authors upon request.

Code availability

The computer codes for STS fittings are provided with this paper.

References

1. Randeria, M. et al. Crossover from Bardeen-Cooper-Schrieffer to Bose-Einstein condensation and the unitary fermi gas. *Annu. Rev. Condens. Matter Phys.* **5**, 209–232 (2014).
2. Chen, Q. et al. BCS–BEC crossover: From high temperature superconductors to ultracold superfluids. *Phys. Rep.* **412**, 1–88 (2005).
3. Nozieres, P. et al. Bose condensation in an attractive fermion gas: From weak to strong coupling superconductivity. *J. Low. Temp. Phys.* **59**, 195–211 (1985).
4. Nakagawa, Y. et al. Gate-controlled BCS-BEC crossover in a two-dimensional superconductor. *Science* **372**, 190–195 (2021).
5. Kasahara, S. et al. Field-induced superconducting phase of FeSe in the BCS-BEC cross-over. *Proc. Natl Acad. Sci. USA* **111**, 16309–16313 (2014).
6. Kasahara, S. et al. Giant superconducting fluctuations in the compensated semimetal FeSe at the BCS–BEC crossover. *Nat. Commun.* **7**, 12843 (2016).
7. Lin, H. et al. Real-space BCS-BEC crossover in FeSe monolayers. *Phys. Rev. B* **107**, 104517 (2023).
8. Wang, Q.-Y. et al. Interface-induced high-temperature superconductivity in single unit-cell FeSe films on SrTiO₃. *Chin. Phys. Lett.* **29**, 037402 (2012).

9. Zhang, W.-H. et al. Direct observation of high-temperature super-conductivity in one-unit-cell FeSe films. *Chin. Phys. Lett.* **31**, 017401 (2014).

10. Lee, J. J. et al. Interfacial mode coupling as the origin of the enhancement of T_c in FeSe films on SrTiO3. *Nature* **515**, 245–248 (2014).

11. Tan, S. et al. Interface-induced superconductivity and strain-dependent spin density waves in FeSe/SrTiO3 thin films. *Nat. Mater.* **12**, 634–640 (2013).

12. He, S. et al. Phase diagram and electronic indication of high-temperature superconductivity at 65 K in single-layer FeSe films. *Nat. Mater.* **12**, 605–610 (2013).

13. Xu, Y. et al. Spectroscopic evidence of superconductivity pairing at 83 K in single-layer FeSe/SrTiO3 films. *Nat. Commun.* **12**, 2840 (2021).

14. Pedersen, A. K. et al. Interfacial superconductivity in FeSe ultrathin films on SrTiO3 probed by in situ independently driven four-point-probe measurements. *Phys. Rev. Lett.* **124**, 227002 (2020).

15. Faeth, B. D. et al. Incoherent cooper pairing and pseudogap behavior in single-layer FeSe/SrTiO3. *Phys. Rev. X* **11**, 021054 (2021).

16. Kosterlitz, J. M. et al. Ordering, metastability and phase transitions in two-dimensional systems. *J. Phys. C: Solid State Phys.* **6**, 1181–1203 (1973).

17. Beasley, M. R. et al. Possibility of vortex-antivortex pair dissociation in two-dimensional superconductors. *Phys. Rev. Lett.* **42**, 1165–1168 (1979).

18. Epstein, K. et al. Vortex-antivortex pair dissociation in two-dimensional superconductors. *Phys. Rev. Lett.* **47**, 534–537 (1981).

19. Reyren, N. et al. Superconducting interfaces between insulating oxides. *Science* **317**, 1196–1199 (2007).

20. Raychaudhuri, P. et al. Phase fluctuations in conventional super-conductors. *J. Phys.: Condens. Matter* **34**, 083001 (2022).

21. Khestanova, E. et al. Unusual suppression of the superconducting energy gap and critical temperature in atomically thin NbSe2. *Nano Lett.* **18**, 2623–2629 (2018).

22. Fan, Q. et al. Plain s-wave superconductivity in single-layer FeSe on SrTiO3 probed by scanning tunnelling microscopy. *Nat. Phys.* **11**, 946–953 (2015).

23. Gong, G. et al. Oxygen vacancy modulated superconductivity in monolayer FeSe on SrTiO3−δ. *Phys. Rev. B* **100**, 224504 (2019).

24. Liu, C. et al. Tuning stoichiometry and its impact on super-conductivity of monolayer and multilayer FeSe on SrTiO3. *Phys. Rev. B* **101**, 140502 (2020).

25. Jiao, X. et al. Post-growth Fe deposition on the superconductivity of monolayer FeSe films on SrTiO3−δ. *Phys. Rev. Mater.* **6**, 064803 (2022).

26. Halperin, B. I. et al. Resistive transition in superconducting films. *J. Low. Temp. Phys.* **36**, 599–616 (1979).

27. Liu, C. et al. High-order replica bands in monolayer FeSe/SrTiO3 revealed by polarization-dependent photoemission spectroscopy. *Nat. Commun.* **12**, 4573 (2021).

28. Benfatto, L. et al. Broadening of the Berezinskii-Kosterlitz-Thouless superconducting transition by inhomogeneity and finite-size effect. *Phys. Rev. B* **80**, 214506 (2009).

29. Blatter, G. et al. Vortices in high-temperature superconductors. *Rev. Mod. Phys.* **66**, 1125–1388 (1994).

30. Liu, Z. et al. Effects of domain structures on vortex state of two-dimensional superconducting Mo2C crystals. *2D Mater.* **6**, 021005 (2019).

31. Liu, Y. et al. Spatial inhomogeneity of superconducting gap in epitaxial monolayer FeTe$_{1-x}$Se$_x$ films. *Phys. Rev. B* **108**, 214514 (2023).

32. Kang, B. L. et al. Preformed Cooper pairs in layered FeSe-based superconductors. *Phys. Rev. Lett.* **125**, 097003 (2020).

33. Sprau, P. O. et al. Discovery of orbital-selective Cooper pairing in FeSe. *Science* **357**, 75–80 (2017).

34. Huang, D. et al. Monolayer FeSe on SrTiO3. *Annu. Rev. Condens. Matter Phys.* **8**, 311–336 (2017).

35. Liu, C. et al. Heterostructural one-unit-cell FeSe/SrTiO3: from high-temperature superconductivity to topological states. *2D Mater.* **7**, 022006 (2020).

36. Zhang, H. et al. Sign changing pairing in single layer FeSe/SrTiO3 revealed by nonmagnetic impurity bound states. *Commun. Phys.* **3**, 1–8 (2020).

37. Misawa, T. et al. Ab initio evidence for strong correlation associated with Mott proximity in iron-based superconductors. *Phys. Rev. Lett.* **108**, 177007 (2012).

38. Cui, W. et al. An in situ electrical transport measurement system under ultra-high vacuum. *Rev. Sci. Instrum.* **91**, 063902 (2020).

39. Hasegawa, S. et al. Electronic transport at semiconductor surfaces––from point-contact transistor to micro-four-point probes. *Surf. Sci.* **500**, 84–104 (2002).

40. Kanagawa, T. et al. Anisotropy in conductance of a quasi-one-dimensional metallic surface state measured by a square micro-four-point probe method. *Phys. Rev. Lett.* **91**, 036805 (2003).

Acknowledgements

Author contributions

D.-P.Z., Y.W., L.W. and Q.-K.X. designed and coordinated the experiments. D.-P.Z., W.C., Y.L., G.G., L.Z., G.J. and Y.Z. conducted film growth, STM/STS and transport measurements. X.H., D.Z., W.L., S.J., K.H. and X.M. participated in the data analysis. W.C. and Y.L. plotted the figures. D.-P.Z., L.W. and Q.-K.X. wrote the manuscript. All authors discussed the results and commented on the manuscript.

Competing interests

The authors declare no competing interests.

Additional information

Supplementary information The online version contains supplementary material available at https://doi.org/10.1038/s41467-024-47350-0.

Correspondence and requests for materials should be addressed to Yilin Wang, Lili Wang or Qi-Kun Xue.

Peer review information *Nature Communications* thanks the anonymous, reviewer(s) for their contribution to the peer review of this work. A peer review file is available.

Reprints and permissions information is available at http://www.nature.com/reprints